

Power grid frequency data base

Richard Jumar^{1*}, Heiko Maaß¹, Benjamin Schäfer²,
Leonardo Rydin Gorjão^{3,4}, and Veit Hagenmeyer¹

May 10, 2022

1. Karlsruhe Institute of Technology - Institute for Automation and Applied Informatics (IAI), Germany
 2. School of Mathematical Sciences, Queen Mary University of London, United Kingdom
 3. Forschungszentrum Jülich, Institute for Energy and Climate Research - Systems Analysis and Technology Evaluation (IEK-STE), Germany
 4. Institute for Theoretical Physics, University of Cologne, Germany
- * corresponding author: Richard Jumar (richard.jumar@kit.edu)

Abstract

The transformation of the electrical energy system due to the increasing infeed from renewable energy sources has attracted much attention in diverse research communities. Novel approaches for grid control, grid modeling, and grid architectures are widely proposed. However, data from actual power system operation are rarely available but are critically necessary to analyze real-world scenarios or to evaluate models. In the present paper, we introduce a precisely time-stamped data set comprising power grid frequency measurements from twelve independent synchronous areas of different sizes in one-second resolution. Furthermore, the data includes a synchronized measurement of the frequency within the Continental European synchronous area with measurement points in Portugal, Germany, and Turkey, maximizing the geographical span. Finally, we provide excerpts of the underlying raw data. Data were collected using a self-developed Phasor-Measurement-Unit(PMU)-like device, the Electrical Data Recorder (EDR), connected mostly to conventional low-voltage power outlets.

1 Background & Summary

For the actual transformation of the energy system, energy research should be transparent to enable scientific discussion, but also particularly for providing information to policymakers or the general public.¹ In this context, a real-world power grid frequency open data base can be valuable to understand state-of-the-art power systems but also to help to advance the transition towards fully renewable power systems. Recording the power grid frequency is particularly

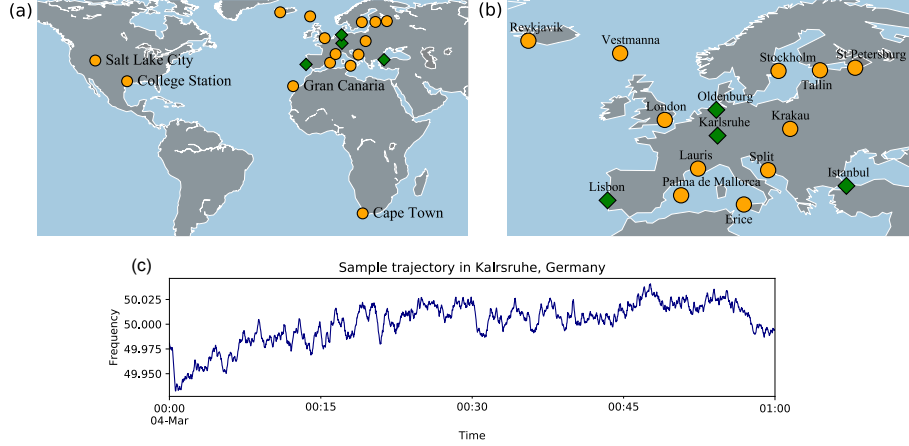


Figure 1: Overview of available data. (a): A (partial) world map shows the different locations at which measurements were taken. Australia and large parts of Asia are not shown as there were no measurements recorded. (b): Zoom of the European region (not showing Gran Canaria). Circles indicate measurement sites where single measurements for several days were taken, diamonds mark the four locations where we performed synchronized measurements in the Continental European system for one month. (c): Sample frequency trajectory, recorded in Karlsruhe, Germany. Maps were created using Python 3 and geoplots.

interesting as it reflects the balance of supply and demand.² Hence, it allows insights into fluctuations of consumers and (also renewable) generators.³ Furthermore, the frequency is widely used for balancing and control actions, as well as a measure of the power system’s stability.² Finally, frequency dynamics are highly regulated by the transmission system operators (TSOs)⁴ and influenced by market activities.⁵ Moving towards a fully sustainable power system, we should thus understand current power systems. Specifically, to which extent specific regulations, energy mixes, consumer fluctuations, etc. impact the frequency dynamics, and thereby grid stability. This understanding is crucial to implement new smart grid concepts,⁶ such as modern demand response concepts,⁷ the introduction of *flexurers*,⁸ or to make theoretical predictions, such as: How do fluctuations impact the grid’s stability^{9,10}? Specifically, how far does the size of a synchronous area —like in island grids or potentially small microgrids^{11,12} —has an impact on the frequency stability issues and control efforts to care for? How do fluctuations spread within one synchronous area^{13,14}? When is a power grid susceptible to cascading failures and how do these propagate^{15–18}? While some of these questions have been touched upon by previous wide-area synchronized measurements,^{19–21} no easily accessible open data are available for such synchronized wide-area measurements. Even more so, data form differently sized synchronous regions to validate scaling laws and investigate the impact of microgrids have, to our knowledge, not been provided openly

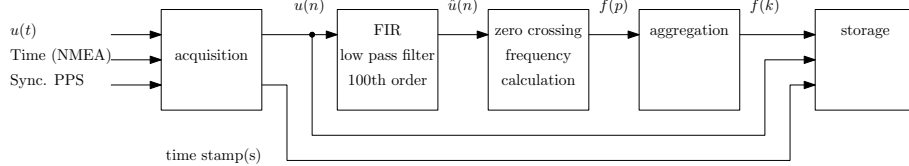


Figure 2: Logic representation of the data flow: From continuous voltage input $u(t)$ to one-second aggregates of the power grid frequency $f(k)$.

and only TSOs of large synchronous areas, such as Continental Europe or Great Britain, disclose such data publicly.^{22,23} Academic and spin-off projects to acquire power grid measurement data already exists: Well known are FNET/-GridEye,²⁴ Grid Radar,²⁵ and mainsfrequency.com²⁶ but none of the existing projects offer openly available databases, which limits their scientific value.

Therefore, in the present paper, we introduce a first open data base of measurements of the power grid frequency recorded in the period 2017 to 2020 in various European and some non-European synchronous areas. Measurement locations are highlighted on a map in Figure 1. The focus lies on covering multiple synchronous areas of different size, ranging from small regions, such as the Faroe Islands with approximately fifty thousand inhabitants, to the Continental European synchronous area with about half a billion inhabitants. Furthermore, we conducted a synchronized measurement at four different locations within the continental European synchronous area for a full month. Overall, we offer 428 days of recorded frequency trajectories in a generally applicable CSV format as well as sample raw data using the original 25 kHz sampling of the sinusoidal voltage signal recorded at a given connection point.

Accompanying this publication, we present an initial data analysis that focuses scaling and spatio-temporal properties of power grid frequency measurements.²⁷

2 Methods

In the following we describe the details of data acquisition as well as the signal processing used to generate the time series provided in this data set. We perform data acquisition using the Electrical Data Recorder (EDR).^{28–30} The device reports and stores time-stamped frequency measurements, similar to a Phasor Measurement Unit (PMU). Additionally, it is capable of storing raw data, i.e., the full time series of samples of the underlying electrical signal. The acquisition time is referenced to the Coordinated Universal Time (UTC), using the timing information provided by the satellite-based Global Positioning System (GPS) and its high resolution Pulse Per Second (PPS) signal. Figure 2 depicts a logical representation of the signal and data flow within the instrument.

2.1 Acquisition

In this section we describe the data acquisition procedure from the physical input signal to the discrete samples. We acquire the voltage at the connection point, which is continuous in time t . The signal is subsequently limited in bandwidth, scaled, and continuously sampled using a 16 bit analog-digital-converter (ADC) at a nominal sampling frequency f_s of 25 kHz¹. This process results in a series of discrete sampled values $u(n)$ spaced $1/f_s$ on the time axis. Since f_s is provided by a quartz oscillator within the ADC it is accurate to around ± 100 ppm.

More accurate timing information is provided by an accompanying GPS receiver in two different ways: Second level timestamps are derived from the standardized NMEA 0183 messages, sent by the receiver once per second as string of ASCII characters. The temporal alignment of each sample $u(n)$ is provided by evaluating the receiver's PPS signal. Technically, we feed the low-pass filtered PPS and $u(t)$ to synchronously captured ADC channels to eliminate delay inconsistencies between the signals. Processing of the samples is performed in blocks of a duration of one second. Timestamps are assigned to these blocks by the software based on the slope (rising edge) of the PPS.³⁰ This results in secondly stamped raw and frequency data, which are subsequently buffered on local hard drive and sent to a large-scale storage when an internet connection is available. Sampling, evaluation, and storage are designed for continuous long-term time-stamped full-sample data recording without interruptions.

2.2 Frequency Calculation

Following the processing chain (Figure 2) the digital signal is conditioned prior to the frequency calculation. Signal conditioning aims at removing distortions (harmonics, injections from photo voltaic inverters, voltage transients, etc.) from the wave form. In frequency domain this is equivalent to limiting the signals bandwidth to include only the interesting frequency deviations. The raw samples $u(n)$ are therefore low-pass filtered using a Finite Impulse Response (FIR) filter. Exploiting the linear phase response of this filter class, the constant group delay is counteracted by shifting the sample indices accordingly. Hence, there is no resulting delay between the input $u(n)$ and the filtered output $\tilde{u}(n)$. The filter length L and coefficients $h(n)$ are selected based on the nominal power grid frequency f_{nom} which can be 50 Hz or 60 Hz and the sampling rate f_s . Choosing $L = f_s/5f_0 \cdot 2$ we get an even order filter. Weighing the kernel function

$$h(n) = \begin{cases} 2\pi \cdot 2f_{\text{nom}}/f_s, & \text{for } n = N/2, \\ \frac{\sin(2\pi \cdot 2f_{\text{nom}}/f_s(n-L/2))}{n-L/2}, & \text{otherwise} \end{cases} \quad (1)$$

with a Hamming window results in a filter with its 3 dB corner frequency close to f_{nom} . For 25 kHz sampling frequency and 50 Hz nominal frequency, this leads to a filter with $L = 100$.

¹ The sampling rate is adjustable. In a few cases we set the rate to 12.8 kHz to save disc space and to make longer recordings.

Table 1: Number of aggregated measurements (periods) per second depending on the power grid frequency

Frequency	Periods	Frequency	Periods
$49 \text{ Hz} \leq f < 50 \text{ Hz}$	50, 51	$59 \text{ Hz} \leq f < 60 \text{ Hz}$	60, 61
$50 \text{ Hz} \leq f < 51 \text{ Hz}$	49, 50	$60 \text{ Hz} \leq f < 61 \text{ Hz}$	59, 60

Applying this filter to the raw data $u(n)$ we obtain the filtered $\tilde{u}(n)$ and calculate the current grid frequency by evaluating the time between two subsequent inclining zero-crossings (ZC) of the waveform. Since the samples of the input signal will not coincide with actual point in time of the ZC, we linearly interpolate between two adjacent samples of a ZC to find the exact time of intersection with the zero line. Figure 3 shows in detail which samples are included in the process. This results in one frequency value $f(p)$ per period p of the input signal.

Next, we have to chose an appropriate method of aggregation to provide one frequency reading per second. Although trivial at first sight, aggregation has its challenge: The periods are usually not aligned with the interval given by a UTC second. It is therefore important to consider the alignment of input signal and timestamp reference (i.e., the beginning of a second) to decide which periods p belong to a aggregation interval k . In our approach, the last inclining ZC before the start of a new second opens the interval. It is closed with the completion of the last full period within the second, i.e., the last inclining ZC before the next second. This ZC is also the first for the following interval, and so on. The number of periods that are aggregated to form a secondly average therefore varies with the phase of the input signal and its frequency, see Table 1.

2.3 Code availability

The code that is required to operate the EDR acquisition device is not openly available, since the development of hardware and software is still ongoing. The MATLAB code for generating the graphics and analyses in this paper is available along with the data.³¹ We use MATLAB Version 2020a.

3 Data Records

The file-based data records are available online under <https://osf.io/by5hu/>.³¹ We provide two sub directories: *raw* containing raw data excerpts; and *frequency* containing the frequency data in one-second resolution.

We use a two-letter code (like DE for Germany) in accordance with the ISO 3166 to designate the regions in which the measurements were taken. Table 4 maps the abbreviations to the campaigns, the regions, and the files. In some regions we conducted multiple campaigns in different locations. These are differentiated by adding a sub region code specific to the location. For example,

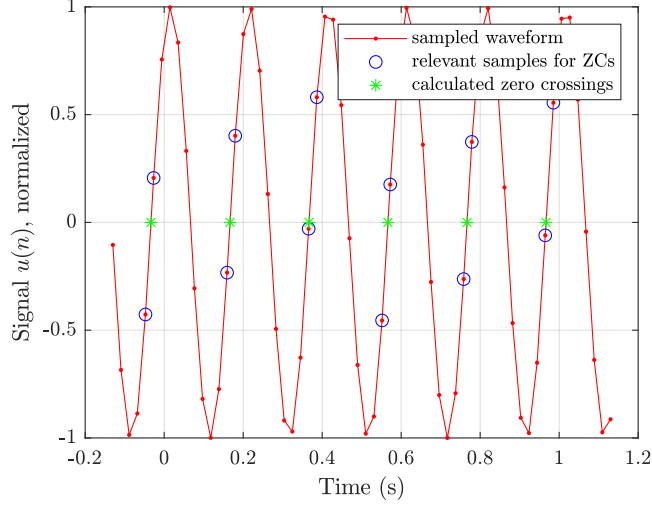
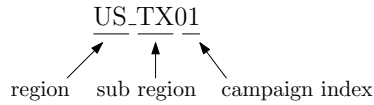


Figure 3: We determine the power grid frequency from the captured samples as the reciprocal of the duration between rising zero-crossings (ZCs). Exact times of ZCs (asterisks) are calculated from the two adjacent samples (circles) to the ZC using linear interpolation. The last ZC before the beginning of a second (at $t = 0$) is the first ZC included in the secondly average value. For this illustration we chose the signal frequency (5 Hz) and sampling frequency (50 Hz) much lower than in the actual acquisition system.

data recorded in Karlsruhe (Germany) are identified by the key DE_KA. As we intend to continue data collection, the filenames also carry an index as campaign identifier. An example filename construction looks like this:



3.1 Frequency Data

For the isolated measurements (e.g. on islands) we provide one file per campaign, including timestamp and frequency trajectory. Files of measurements within the Continental European synchronous area (EC) also contain the frequency measured in Karlsruhe together with a common timestamp. The data of the synchronized campaign including the measurements from Lisbon (Portugal), Oldenburg and Karlsruhe (Germany), as well as Istanbul (Turkey) are located in a single file (SYNC01.csv) using a common timestamp.

Frequency data are provided as CSV of the format shown in Table 2. We use a semicolon delimiter. The frequency columns are marked with ‘f50’ or ‘f60’

Table 2: Data format of CSV files containing the frequency time series. Delimiter: Semicolon. Total number of columns depends on data set.

Col.	Head	Description	Format
1	Time	Date and time, UTC	yyyy-MM-dd HH:mm:ss
2	f50_'loc'	$f - f_{\text{nom}}$ at 'loc' (mHz)	decimal: -123.456
3	QI_'loc'	Quality indicator for 'loc' series	integer (0...3)
4	f50_'loc'	$f - f_{\text{nom}}$ at 'loc' (mHz)	decimal: -123.456
5	QI_'loc'	Quality indicator for 'loc' series	integer (0...3)

according to the nominal frequency in the measurement location, i.e., 50 Hz or 60 Hz, respectively. We always report the difference of the measured frequency f and nominal frequency f_{nom} in mHz. So f50 is

$$\text{f50} = (f - 50 \text{ Hz}) \times 10^{-3} \quad (2)$$

To ease (partial) data import, each line carries a full timestamp. The timestamps are guaranteed to be regular, so they are equidistant with one second spacing and unique. Therefore, they may be omitted to speed up the import. Besides the timestamp, all data are numbers using a period as decimal limiter.

Data points that were corrupted during the acquisition, e.g. by the loss of GPS reception, are linearly interpolated. The user can distinguish these points by evaluating the column of the quality indicator (QI) described in Table 3.

Table 3: Quality indicator (QI) for frequency data

QI	Description
0	Data OK (as specified)
1	Invalid data (only in synchronous campaign)
2	Interpolated data

In the Continental European synchronized campaign (Karlsruhe (Germany), Oldenburg (Germany), Turkey, Portugal) not all frequency recordings begin and end at the same time. The file begins with the start of the first recording and stops with end of the last recording. Consequently, there are times for which some of the data are not available. At these times, entries in the affected frequency columns are filled with zeros and are marked as “invalid data” in the corresponding quality indicator column.

3.2 Raw Data

Despite the focus of the data base on pre-processed frequency data, we also provide excerpts of raw data, i.e., the sampled waveform of the voltage at the connection point of the EDR. Each excerpt contains an one hour recording at

Table 4: Keys of measurement locations and their connection to synchronous areas. For each country, we adopt the ISO 3166 code and further specify the region or city when multiple measurements were recorded in the same country. Devices are connected at power sockets, except for DE_KA. PCC stands for point of common coupling.

Key	File names	Measurement location	Synchronous area	Environment
Islands				
IS	IS01	Reykjavík, Iceland	Iceland	Hotel
FO	FO01	Vestmanna, Faroe Islands	Faroe Islands	Hotel
ES_GC	ES_GC01 ES_GC02	Las Palmas de Gran Canaria, Canary Islands, Spain	Gran Canaria	Hotel
ES_PM	ES_PM01	Palma de Mallorca, Balearic Islands, Spain	Mallorca	Office
Continental				
DE_KA	SYNC01	Karlsruhe, Germany	Continental Europe (CE)	Office, PCC
DE_OL	SYNC01	Oldenburg, Germany	CE	Home
TR	SYNC01	Istanbul, Turkey	CE	Office
PT	SYNC01	Lisbon, Portugal	CE	Home
FR	FR01	Lauris, France	CE	Home
HR	HR01	Split, Croatia	CE	Hotel
PL	PL01	Krakau, Poland	CE	Hotel
IT	IT01	Erice, Sicily, Italy	CE	Hotel
GB	GB01 GB02	London, United Kingdom	Great Britain	Home
EE	EE01	Tallinn, Estonia	Baltic	Office
SE	SE01	Stockholm, Sweden	Nordic	Hotel
Others				
US_UT	US_UT01	Salt Lake City, Utah, US	Western Interconnection	Hotel
US_TX	US_TX01 US_TX02	College Station, Texas, US	Texas Interconnection	Hotel
ZA	ZA01	Cape Town, South Africa	South Africa	Hotel
RU	RU01	St. Petersburg, Russia	Russia	Hotel

25 kHz sampling frequency from all synchronous areas. Raw data are provided as a CSV file with one voltage entry per time step, which is $1/f_s = 40 \mu\text{s}$. To reduce overhead, the files do not contain timing information. Instead, the file name carries the timestamp of the first sample in the file, from which the user may reconstruct the time vector.

It is important to note that the polarity and phase (either L1, L2, or L3 in three-phase power systems) of the raw data should be considered unknown. If the absolute phase angle matters, the user might have to correct the phase using a local reference. In location DE_KA we assume be connected to phase one (L1) in correct polarity, but no guarantees can be made.

4 Technical Validation

In the following sections we present methods and results for the validation of this data set. We begin by comparing the recorded data from multiple instances of our instrument with each other and with external sources to quantify the error in the typical recording conditions. Subsequently, errors and limitations of our frequency calculation algorithm are discussed in a broader form. This discussion is motivated by the fact that there is no general concept of what the true frequency of a distorted (non-sinusoidal) signal is. We close with remarks on the data quality in terms of total data amount and share of missing data.

4.1 Comparative frequency measurements

To evaluate the performance of our frequency measurements in actual measurement conditions, we prepare a comparative setup. Two EDR instruments are placed next to each other with their GPS receivers located in close proximity. They are connected to the same power outlet but plugged in opposite polarities. Using this set-up we record the grid frequency simultaneously for approximately 10 hours with both devices. We get two frequency time series, f_1 and f_2 . The recording interval is from ‘2019-06-27 20:10’ to ‘2019-06-28 06:50’ and its data are available along with the data set. Using the timestamp we compare both recordings. Rows with missing data are discarded.

Figure 4 (a) depicts the empirical error distribution from this test. We find a mean error of -34 nHz and an RMSE of $78 \mu\text{Hz}$. The maximum deviation in the experiment is $443 \mu\text{Hz}$, the median $45 \mu\text{Hz}$, and the 99th percentile $236 \mu\text{Hz}$. Analyzing the deviations $f_1 - f_2$ in frequency domain shows several distinct peaks and an increase in amplitude towards higher frequencies, see Figure 4 (b). None of the peaks relates to any known process or process cycle within the acquisition or signal processing. Since the amplitude of the individual spectral components is small compared to the RMSE, the error is not dominated by a single periodic mechanism.

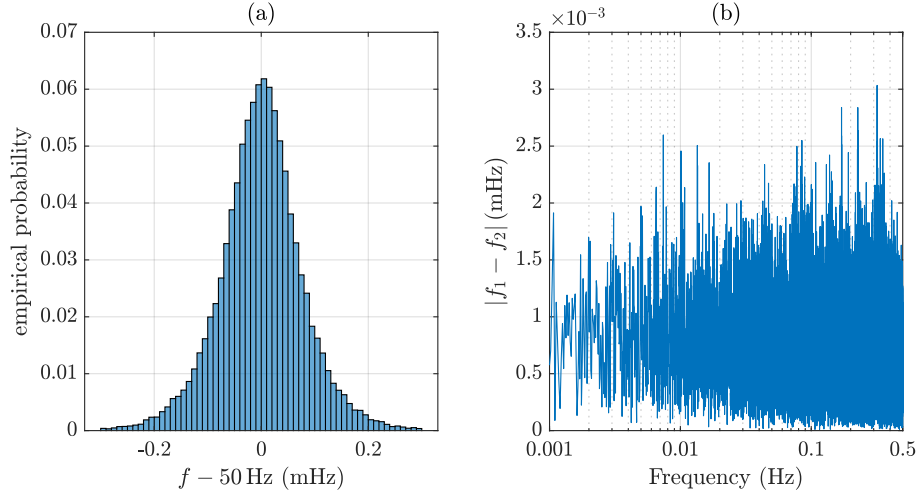


Figure 4: Comparing the frequency records of two EDR instruments from the same location: a) Histogram of the frequency differences. b) Single-sided amplitude spectrum of the frequency differences.

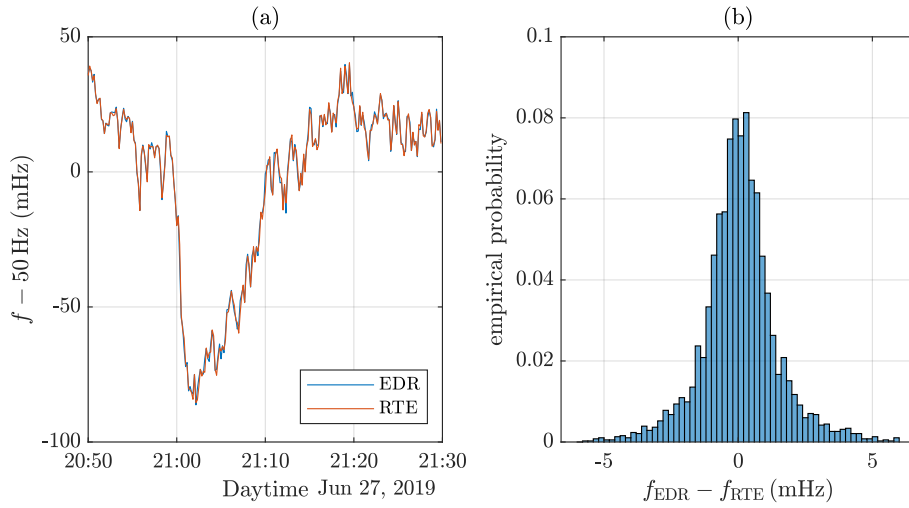


Figure 5: Comparison of EDR and RTE measurements for a 10 hour recording: a) Visual comparison of an excerpt, showing a close match. b) Histogram of the differences showing the error distribution.

4.2 Comparison with external data source

In the following we compare data from an external source from the same synchronous region with our recordings. This experiment intends to show any temporal alignment mismatches and to give a general idea of how expected differences to other sources might look like. Deriving measurement accuracy from this experiment is not advisable since a) the measurement locations differ and b) we have no knowledge about how and to what accuracy the external system performs. Physical effects in the power distribution add indistinguishably to the measurement errors.

For the Continental European synchronous area the french TSO Réseau de Transport d'Electricité (RTE) provides frequency times series in 10-second resolution.³² We compare the RTE data to our own measurements by aggregating our data also to a 10 second resolution. We use the same data as for the EDR-to-EDR comparison in Section 4.1. Since the timestamp of the RTE data is aligned in the center of the aggregation window, we have to adjust our time series to match this scheme.

Figure 5 compares the two frequency time series. Figure 5 a) depicts an excerpt of both time series, which shows that the trajectories match well on visual inspection. Calculating the sample by sample difference leads to an RMSE of 1.57 mHz. The histogram of the deviations is depicted in Figure 5 b). The error is roughly an order of magnitude larger than what we have observed directly comparing two of our instruments. This may be caused by the reasons indicated above.

4.3 Discussion on the frequency estimation technique

The ZC algorithm implicitly defines frequency as the inverse of period length between zero-crossings. Consequently, it establishes frequency as quantity that is only defined at specific points in time, namely the zero-crossing. This definition is very different from the form used to define a sinusoidal signal:

$$u(t) = A_{\text{nom}} \sin(2\pi f_{\text{nom}} t + \varphi(t)), \quad (3)$$

with the variable phase angle $\varphi(t)$ and the amplitude A_{nom} . In a sense, the ZC algorithm implements a sampling of the frequency, which is important for the following discussion.

There are four major aspects that influence the quality of the frequency estimation using the EDR and the presented ZC algorithm. These are:

1. Disturbances on the power signal
2. Phase sensitivity of frequency calculation
3. Temporal alignment between instruments
4. Stability of the clock reference

Disturbances on the power signal Disturbances on the power signal cause the input waveform to differ from a sine, which leads to errors in determining the proper moment when the signal crosses zero. Static harmonics of any order distort the waveform, but they do not alter the length of periods. As most of the harmonic content is filtered out during signal processing, it does not influence the accuracy of the estimation.

On the contrary, any random signal that passes the filtering will cause frequency estimation errors, also on the aggregated level. To investigate this influence, we synthetically generate sinusoidal signals with superimposed white noise of different power levels. We use a signal length of one hour and pass the samples through the processing chain, shown in Figure 2.

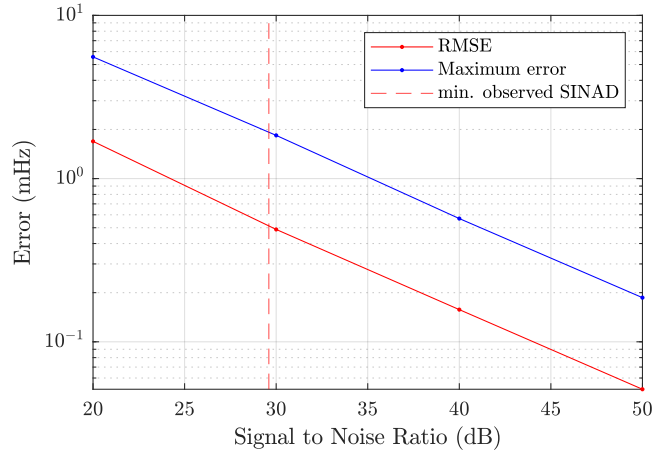


Figure 6: Deviation of the ZC frequency estimate due to additive white noise in signal input. We use $f_{\text{nom}} = 50 \text{ Hz}$ as input frequency and one-hour of synthetic data. Vertical line: Lowest Signal to Noise and Distortion ratio (SINAD) observed in the measurement campaigns ($\text{SE01} = 29.6 \text{ dB}$).

Figure 6 depicts the observed maximum error and RMSE of the frequency estimate over the Signal to Noise Ratio (SNR). The vertical line indicates the lower limit of the Signal to Noise and Distortion Ratio (SINAD) over all measurement campaigns. In this setting, we count all distortions as noise although the harmonics dominate in the measurement campaigns. The rationale is to apply the reproducible albeit harder test case.

The test results in an maximum error of 2 mHz and an RMSE of 0.5 mHz in the given measurement scenarios. Thus, signal distortion is one of the major contributors to the total error in relation to the following error sources.

Phase sensitivity of frequency calculation The ZC algorithm relies on detecting inclining ZCs. Therefore, the absolute phase (phase with respect to UTC) of the signal determines which of the period-wise frequency measurements $f(p)$ are aggregated to form a one-second-reading $f(k)$. This behavior represents

an error in the sense that two instruments can report different frequencies depending on the phase of the signal. The difference is a direct consequence of the non-continuous definition of the frequency used in the ZC algorithm. This effect occurs, for instance, if one instrument is plugged into a power socket reversely compared to another. The series of periods that is included into $f(k)$ by this instrument begins half a period later or earlier (± 10 ms in a 50 Hz system) compared to the other one. This misalignment results in a frequency error when comparing the two aggregated frequency measurements from those two instruments.

The difference between the *true* one-second average of the grid frequency and the estimation $f(k)$ is hard to quantify, as it depends on the momentary phase of the input signal. We approach this issue by running a simulation for which we generate artificial samples that we pass through our signal processing chain (Figure 2).

Via a frequency modulator, we can generate a realistic but synthetic signal for which we know the frequency exactly. Further, shaping the spectrum of the modulation signal allows to investigate the influence of spectral components of the frequency changes on the precision of the estimation.

We begin by defining the momentary or instantaneous frequency $f_i(t)$ of a sinusoidal signal

$$f_i(t) = f_{\text{nom}} + \frac{1}{2\pi} \frac{d}{dt} \varphi(t). \quad (4)$$

Frequency modulation is now characterized by

$$f_i(t) - f_{\text{nom}} = D_f m(t), \quad (5)$$

where D_f is the modulation depth and $m(t)$ some modulation signal. To apply frequency modulation, i.e., to change $f_i(t)$ in dependence of $m(t)$, the phase $\varphi(t)$ has to be

$$\varphi(t) = 2\pi D_f \int_{-\infty}^t m(\tau) d\tau. \quad (6)$$

As we are operating in discrete time domain, we generate samples of a frequency modulated band pass signal by using the trapezoidal approximation for the integral in (6). The frequency modulated test signal $u_{\text{test}}(n)$ is therefore

$$u_{\text{test}}(n) = A_{\text{nom}} \sin \left(\frac{n}{f_s} 2\pi f_{\text{nom}} + 2\pi D_f \frac{1}{2} \sum_{\theta=1}^n \frac{m(\theta-1) + m(\theta)}{f_s} \right). \quad (7)$$

To judge the quality of the one-second average estimate $f(k)$, we define the true one-second average of the frequency of the signal $u_{\text{test}}(n)$ as

$$\bar{f}_{\text{test}}(k) = \frac{1}{N} \sum_{n=kN+1}^{(k+1)N} f_{\text{nom}} + D_f m(n) \quad \text{for } k = 0, 1, 2, \dots, \quad (8)$$

which is the secondly average *regardless* of the current phase of the signal.

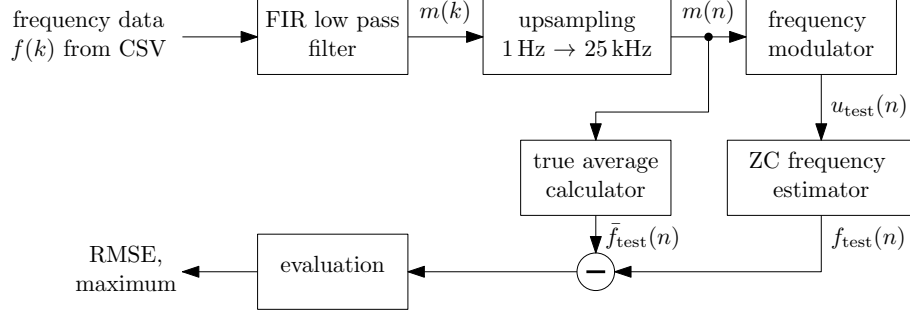


Figure 7: Logical representation of the experimental setup to estimate the error of the ZC algorithm due to phase sensitivity.

The process (depicted in Figure 7) comprises to take a frequency trajectory (as provided in the CSV files), optionally pass it through a low-pass filter, and use it as $m(n)$ to generate an artificial signal with the same frequency trajectory. Since $m(n)$ is quasi-continuous we can obtain the true one-second frequency average according to (8). These averages are subsequently compared with the results from the ZC algorithm. We calculate the RMSE and maximum deviations over the length of the artificial signal (one hour in our case). Figure 8 presents the results of this study. Figure 8 (a) depicts the power spectrum of the frequency. We choose the data set from the Faroe Islands for its high modulation signal power. Using a low-pass filter we suppress some of the higher frequency content from $m(n)$, while preserving the total signal power. Figure 8 (b) shows the amplitude filter responses. We choose the filters to be FIR with decreasing length, so that the roll-off always has the same steepness. This prevents cross-over in the transition region. Finally, Figure 8 (c) displays the resulting errors in dependence of the chosen cutoff frequency for the low-pass filter. The rightmost point (0.5 Hz) relates to no filtering and is therefore equivalent to the setting of the measurement campaign. Thereby, the maximum error is 1.52 mHz and the RMSE is 0.34 mHz. Increasing the cutoff frequency results in larger error which corresponds to the susceptibility of the ZC algorithm to sudden frequency changes.

The error figures for signal distortion and for phase sensitivity are in the same range (RMSE \approx 0.5 mHz) and are therefore considered to contribute equally to the total deviations in the data set.

Temporal alignment between instruments When comparing aggregated data, the alignment of the underlying sampled time series is critical. Sampling the PPS within the acquisition system results in a static delay (phase offset) due to tolerances of the used electrical components. Therefore, there is a phase shift between the internal clock and UTC. This error does not manifest itself when investigating the frequency data from a single instrument, but shows up when comparing data from two sources. The impact of this delay on the frequency time

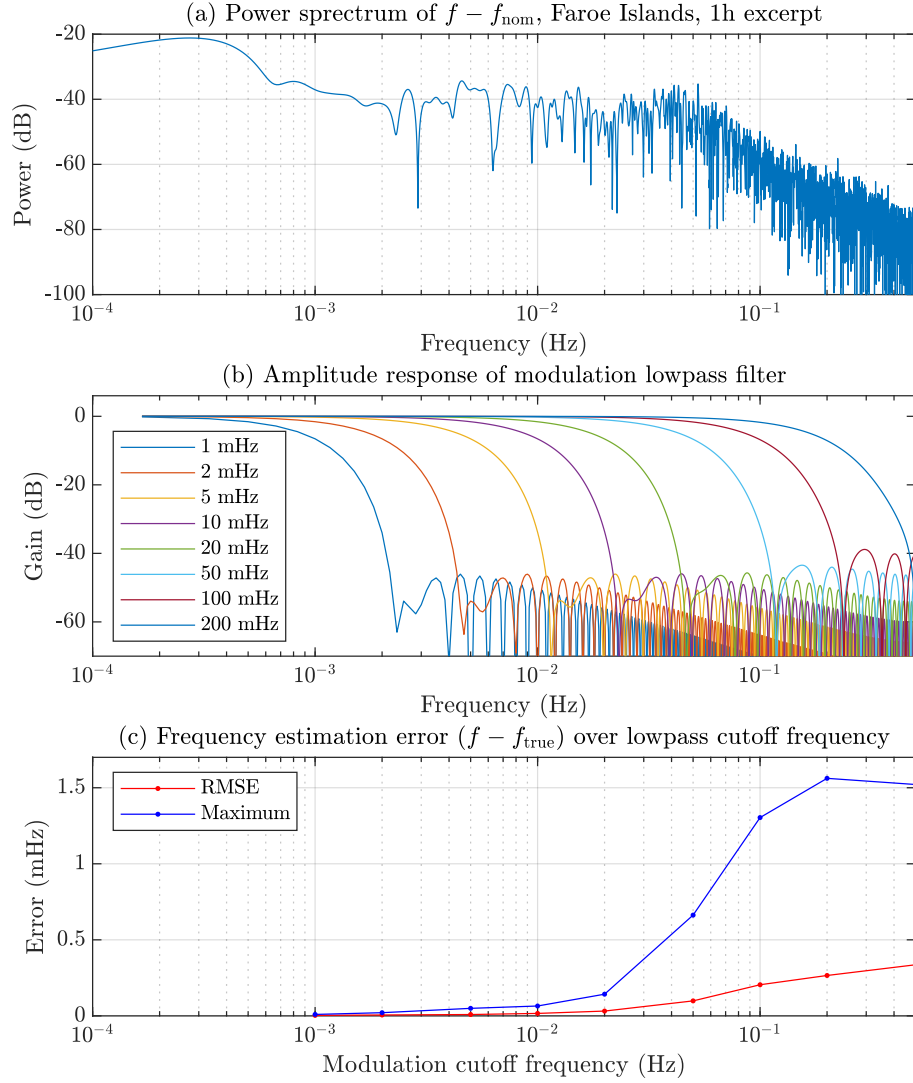


Figure 8: (a) Power spectrum of the frequency deviations, as reported in the CSV files. Here the deviations serve as modulation signal. Spectrum generated using a 2^{16} -point FFT on an one-hour excerpt from the Faroe Island data. (b) Amplitude frequency responses of the FIR low-pass filters used on the modulation signal. Note the constant roll-off steepness for the different cutoff frequencies. (c) Deviation between the true one-second average and the estimated frequency (using the zero-crossing algorithm) in dependence of the low-pass cutoff frequency when applied to a sinusoidal test signal that is frequency modulated with the output of the low-pass filter.

series is dependent on the measured signal. In steady state condition, the effect vanishes and it has increasing influence when the frequency changes rapidly.

We determined that the device specific and static timing offset is $\pm 5 \mu\text{s}$ (3σ).³⁰ Two instruments might therefore be misaligned by $10 \mu\text{s}$ or one quarter of a sample at 25 kHz sampling frequency. As this misalignment is very small compared to the aggregation interval of the frequency time series (one second), it is only marginally contributing to the total error.

Stability of the reference clock The stability of the reference clock is key to keep offsets in the frequency measurements to a minimum. As the frequency is calculated from the time between zero-crossings, the corresponding frequency error Δf to a given uncertainty in the time Δt is

$$\Delta f = \left| -\left(t = 1/f_{\text{nom}}\right)^{-2} \right| \Delta t. \quad (9)$$

The uncertainty in the clock relates to the interval of one period of the input waveform. We use the highly stable PPS signal³³ with $\pm 1 \mu\text{s}$ accuracy to determine the duration of a second in our instrument. Experimentally, we find that the error in steady state conditions over a 10 minute interval is $26.7 \mu\text{Hz}$ at 50 Hz within a 95.4% confidence interval.³⁴ This error is therefore irrelevant compared to the previously discussed error sources.

4.4 Data quality

Despite our greatest efforts, the time series in this data set contain multiple missing entries. Some campaigns are fragmented because we conducted measurements during business or private travels. Other interruptions were caused by a loss of GPS reception. For the majority of short interruptions ($< 10 \text{ s}$) we believe that they originate from acquisition process interruptions caused by the operation system on our device. The share of fully trustworthy data is 97.6 % overall. This number is probably lower than it could be: We decided to be very strict by considering each one-second aggregate as faulty if at least one period measurement was missing. In Table 5 we provide basic information on the campaigns as well as numbers for the share of missing data for each file.

Table 5: Measurement campaign files and properties

File	Begin	End	Duration (d)	Missing (%)	Cont. Days	Cont. Reg. Begin
Islands						
IS01	2017-10-14 17:23:45	2017-10-20 07:54:06	5.6	24.0	0.87	2017-10-18 16:27:12
FO01	2019-11-03 21:50:10	2019-11-10 09:15:06	6.5	33.3	0.03	2019-11-04 05:01:20
ES_GC01	2018-02-04 10:36:57	2018-02-10 21:28:57	6.5	0	6.45	2018-02-04 10:36:57
ES_GC02	2018-11-25 00:00:00	2018-11-26 12:29:44	1.5	42.2	0.28	2018-11-25 00:00:00
ES_PM01	2019-09-29 00:00:00	2019-12-31 23:59:59	94.0	0.02	4.7	2019-11-27 10:17:19
GB01	2019-03-04 10:54:37	2019-03-07 23:59:59	3.5	1.96	1.0	2019-03-06 00:00:00
GB02	2019-11-10 22:36:18	2019-12-31 23:59:58	51.1	0.2	3.8	2019-12-25 07:27:20
Continental synchronous areas in Europe						
SYNC01						
- DE_KA	2019-07-09 00:00:00	2019-08-18 23:59:59	41.0	0.0	41.0	2019-07-09 00:00:00
- DE_OL	2019-07-10 11:09:02	2019-08-07 16:14:00	41.0	0.05	14.7	2019-07-11 21:30:37
- PT	2019-07-09 19:34:40	2019-08-18 09:52:21	41.0	4.4	5.4	2019-08-01 23:30:46
- TR	2019-07-09 21:01:29	2019-08-16 14:12:59	41.0	0.01	3.7	2019-07-31 23:59:55
FR01	2019-04-16 00:00:00	2019-04-27 06:56:17	12.0	1.74	0.24	2019-04-19 05:03:47
HR01	2019-04-09 14:31:34	2019-04-12 09:47:02	4.0	0.0	1.25	2019-04-10 19:12:54
IT01	2019-07-02 20:32:32	2019-07-06 16:46:21	5.0	5.4	0.7	2019-07-05 09:03:29
PL01	2019-04-04 13:05:53	2019-04-07 10:42:55	4.0	0.75	0.66	2019-04-05 03:22:29
EE01	2019-03-25 11:09:11	2019-04-17 07:32:47	22.9	0.0	2.0	2019-03-29 00:00:00
SE01	2019-05-06 14:16:09	2019-05-13 06:54:20	6.7	2.15	0.82	2019-05-09 20:34:30
PT01	2018-02-14 14:33:09	2018-02-21 09:10:00	6.8	0.17	0.23	2018-02-21 01:43:28
Other						
US_UT01	2019-05-19 02:54:06	2019-05-25 11:58:16	6.4	0.4	2.29	2019-05-23 04:58:00
US_TX01	2019-05-15 04:35:36	2019-05-16 15:03:56	1.4	0.18	0.6	2019-05-15 04:35:36
US_TX02	2019-05-20 07:21:15	2019-05-23 23:59:58	3.7	4.04	0.61	2019-05-20 07:28:44
ZA01	2017-11-19 11:33:08	2017-11-28 23:59:59	9.5	33.6	0.89	2017-11-22 03:43:16
RU01	2019-04-30 23:00:17	2019-05-12 07:37:57	13.0	0.01	1.3	2019-05-04 10:23:32
Total:			428.1	2.4		

5 Usage Notes

In the following, we provide some hints for working with the data.

5.1 Import of frequency data

As the frequency time series are provided as CSV, they can be easily directly imported with a variety of software tools. Below we provide code snippets for commonly used programming languages to import the data. After import, one should check that the data were read correctly (with the available precision) by plotting or printing the first couple of entries. The user must take care of the correct interpretation of the timestamp, especially if the data are combined from different sources. This data set solely uses UTC timestamps while data from external sources (e.g. TSOs) commonly use local time.

Matlab:

```
1 %since Matlab Version 2020a, direct import to timetable
2 Data = readtimetable('GB01.csv');
3
4 %before e.g. like this
5 df = importdata("GB01.csv")
6 Time = datetime(df.textdata(2:end,1));
7 header = df.textdata(1,:);
8 data = df.data;
```

Python 3 (using Pandas):

```
1 import pandas as pd
2 Data = pd.read_csv("GB01.csv")
```

R:

```
1 library(zoo)
2 DF <- read.zoo("GB01.csv",
3               tz = "UTC",
4               FUN = paste,
5               index = "Time",
6               FUN2 = as.POSIXct,
7               sep = ";",
8               header = TRUE,)
```

5.2 Restore scale and frequency offset

The data are provided in mHz without the nominal frequency offset. If the application requires the frequency to be in Hz and to include the nominal frequency offset, one needs to restore it by calculating

$$f = f_{50_LOC} \times 10^{-3} + f_{nom}. \quad (10)$$

Thereby, `f50_LOC` are the entries in frequency column in a data set with 50 Hz nominal frequency. One can obtain the nominal frequency of the selected region from the head of the frequency column in CSV file, which reads *f50* or *f60* depending on the nominal frequency.

5.3 Filter by Quality Indicator

The quality indicator should be used to filter the time series according to intended application. For statistical analyses it might be appropriate to eliminate all interpolated and non-valid entries ($QI \neq 2$). In MATLAB this operation (including import) could be performed writing:

```
1 Data = readtimetable('GB01.csv');
2 Data.f50_GB(Data.QI_GB ~= 0) = nan;
3 Data = rmmissing(Data);
```

For observing the trajectories instead, the build-in interpolation might be of help. However, some campaigns of the data set are fragmented, so it is advisable to always plot the quality indicator if continuity of the frequency trajectory matters. We want to point out that the chosen linear interpolation should not yield a perfect imputation of missing values—we simply intend to give users an easy start in exploring this data set.

Acknowledgments

We would like to express our gratitude to everyone who helped to create the data base by connecting the EDR in their hotel room, home, or office: Damià Gomila, Malte Schröder, Jan Wohland, Cigdem Yalcin, Filipe Pereira, André Frazão, Kaur Tuttelberg, Jako Kilter, Hauke Hähne, and Bálint Hartmann. We gratefully acknowledge support from the Helmholtz Association by the Program-Oriented Funding program “Storage and Cross-Linked Infrastructures”, via the joint initiative “Energy System 2050 - A Contribution of the Research Field Energy”, with the grant no. VH-NG-1025, and from the associative “Uncertainty Quantification – From Data to Reliable Knowledge (UQ)” with grant no. ZT-I-0029. This work was performed as part of the Helmholtz School for Data Science in Life, Earth and Energy (HDS-LEE). This project has received funding from the European Union’s Horizon 2020 research and innovation program under the Marie Skłodowska-Curie grant agreement no. 840825.

Author contributions

Conceptualization: RJ, HM, BS, and LRG. Development, construction of the EDR, and campaign logistics: HM and RJ. Conduction of measurement campaigns: BS, LRG, RJ, and HM. Data preparation and reprocessing: RJ and HM. Technical validation: RJ. Original draft preparation: RJ and BS. Review and

editing: HM, BS, LRG, and VH. Supervision: HM and VH. Funding acquisition: VH. All authors have read and agreed to this version of the manuscript.

Competing interests

The authors declare no competing interests.

References

- [1] Pfenninger, S. Energy scientists must show their workings. *Nature* **542**, 393–393 (2017).
- [2] Machowski, J., Bialek, J. & Bumby, J. *Power System Dynamics: Stability and Control* (John Wiley & Sons, Chichester, 2011).
- [3] Schäfer, B., Beck, C., Aihara, K., Witthaut, D. & Timme, M. Non-gaussian power grid frequency fluctuations characterized by Lévy-stable laws and superstatistics. *Nat. Energy* **3**, 119–126 (2018).
- [4] ENTSO-E. Network code on requirements for grid connection applicable to all generators (RfG). <https://www.entsoe.eu/major-projects/network-code-development/requirements-for-generators/> (2013).
- [5] Weißbach, T. & Welfonder, E. High frequency deviations within the european power system—Origins and proposals for improvement. *VGB PowerTech* **89**, 26 (2009).
- [6] Fang, X., Misra, S., Xue, G. & Yang, D. Smart Grids - The new and improved Power Grid: A Survey. *IEEE Commun. Surv. Tutor.* **14**, 944–980 (2012).
- [7] Schäfer, B., Matthiae, M., Timme, M. & Witthaut, D. Decentral Smart Grid Control. *New J. Phys.* **17**, 015002 (2015).
- [8] Bärwaldt, G. Energy revolution needs interpreters. *ATZelectronics worldw.* **13**, 68–68 (2018).
- [9] Schäfer, B. *et al.* Escape routes, weak links, and desynchronization in fluctuation-driven networks. *Phys. Rev. E* **95**, 060203 (2017).
- [10] Hindes, J., Jacquod, P. & Schwartz, I. B. Network desynchronization by non-gaussian fluctuations. *Phys. Rev. E* **100**, 052314 (2019).
- [11] Lasseter, R. H. & Paigi, P. Microgrid: A conceptual solution. In *2004 IEEE 35th Annual Power Electronics Specialists Conference (PESC)*, vol. 6, 4285–4290 (IEEE, 2004).
- [12] Kroposki, B. *et al.* Making microgrids work. *IEEE Power Energy Mag.* **6** (2008).

- [13] Zhang, X., Hallerberg, S., Matthiae, M., Witthaut, D. & Timme, M. Fluctuation-induced distributed resonances in oscillatory networks. *Sci. Adv.* **5**, eaav1027 (2019).
- [14] Hähne, H., Schmietendorf, K., Tamrakar, S., Peinke, J. & Kettemann, S. Propagation of wind-power-induced fluctuations in power grids. *Phys. Rev. E* **99**, 050301 (2019).
- [15] Simonsen, I., Buzna, L., Peters, K., Bornholdt, S. & Helbing, D. Transient dynamics increasing network vulnerability to cascading failures. *Phys. Rev. Lett.* **100**, 218701 (2008).
- [16] Yang, Y., Nishikawa, T. & Motter, A. E. Small vulnerable sets determine large network cascades in power grids. *Science* **358**, eaan3184 (2017).
- [17] Schäfer, B. & Yalcin, G. C. Dynamical modeling of cascading failures in the turkish power grid. *Chaos* **29**, 093134 (2019).
- [18] Nesti, T., Zocca, A. & Zwart, B. Emergent failures and cascades in power grids: a statistical physics perspective. *Phys. Rev. Lett.* **120**, 258301 (2018).
- [19] Vanfretti, L., Bengtsson, S., Perić, V. S. & Gjerde, J. O. Spectral estimation of low-frequency oscillations in the nordic grid using ambient synchrophasor data under the presence of forced oscillations. In *2013 IEEE Grenoble Conference*, 1–6 (IEEE, 2013).
- [20] Tuttlberg, K., Kilter, J., Wilson, D. & Uhlen, K. Estimation of power system inertia from ambient wide area measurements. *IEEE Trans. Power Syst.* **33**, 7249–7257 (2018).
- [21] Chai, J. *et al.* Wide-area measurement data analytics using FNET/GridEye: A review. In *2016 Power Systems Computation Conference (PSCC)* (2016).
- [22] TransnetBW GmbH. Regelenergie Bedarf + Abruf. <https://www.transnetbw.de/de/strommarkt/systemdienstleistungen/regelenergie-bedarf-und-abruf> (2019).
- [23] National Grid ESO. Historic frequency data. <https://www.nationalgrideso.com/balancing-services/frequency-response-services/historic-frequency-data> (2019).
- [24] Power Information Technology Lab, University of Tennessee, Knoxville and Oak Ridge National Laboratory. FNET/GridEye. <http://powerit.utk.edu/fnet.html> (2014). 1 day data set "20140905".
- [25] MagnaGen GmbH. Gridradar - An independent grid monitoring system. <https://gridradar.net/home.html?lang=en> (2020).
- [26] Dr. Gobmaier GmbH. Online-measurement of the utility frequency: The meter. https://www.gobmaier.de/index_en.html (2020).

- [27] Rydin Gorjão, L. *et al.* Open data base analysis of scaling and spatio-temporal properties of power grid frequencies. *arXiv e-prints* (2020). URL <https://arxiv.org/abs/2006.02481>.
- [28] Maaß, H. *et al.* First evaluation results using the new electrical data recorder for power grid analysis. *IEEE Trans. Instrum. Meas.* **62**, 2384–2390 (2013).
- [29] Maaß, H. *et al.* Data processing of high-rate low-voltage distribution grid recordings for smart grid monitoring and analysis. *EURASIP J. Adv. Signal Process.* **2015**, 14 (2015).
- [30] Jumar, R., Maaß, H., Kühnapfel, U. & Hagenmeyer, V. Synchronized continuous high-rate time-series recording in distribution grids for accurate evaluation. In *2019 International Conference on Smart Grid Synchronized Measurements and Analytics (SGSMA)*, 1–8 (2019).
- [31] Jumar, R., Maaß, H., Schäfer, B., Gorjão, L. R. & Hagenmeyer, V. Power grid frequency data base. <https://osf.io/by5hu/> (2020).
- [32] Réseau de Transport d'Électricité (RTE). Network frequency. https://clients.rte-france.com/lang/an/visiteurs/vie/vie_frequence.jsp (2014-2017).
- [33] Niu, X. *et al.* Quality evaluation of the pulse per second (PPS) signals from commercial GNSS receivers. *GPS Solutions* **19**, 141–150 (2015).
- [34] Maaß, H., Çakmak, H. K., Bach, F. & Kühnapfel, U. G. Preparing the electrical data recorder for comparative power network measurements. In *2014 IEEE International Energy Conference (ENERGYCON)*, 759–765 (2014).